Extension of the source scanning technique to curved rectangular panels for the vibroacoustic characterization of structures using wall-pressure plane waves

Augustin Pouye, Cédric Maury, Laurent Maxit

Extension of the Source Scanning Technique to Curved Rectangular Panels for the Vibroacoustic Characterization of Structures using Wall-Pressure Plane Waves

Augustin Pouye[a,b,*], Cédric Maury[b], Laurent Maxit[a]

[a] *INSA Lyon, Laboratoire Vibrations-Acoustique (LVA), UR, 69621 Villeurbanne, France.*
[b] *Aix Marseille Univ, CNRS, Centrale Marseille, Laboratoire de Mécanique et d'Acoustique (LMA), 38 rue Frédéric Joliot Curie, 13013 Marseille, France.*

Abstract

The Source Scanning Technique (SST) is an experimental method used to synthesise the vibroacoustic response of a given structure under random excitations such as the Diffuse Acoustic Field (DAF) and the Turbulent Boundary Layer (TBL) using a single monopole source. It was previously developed and validated for simple plane structures such as Flat Rectangular Panels (FRPs). However, in industrial cases, the structures of interest can be more complex. In this paper, the feasibility of the extension of SST to Curved Rectangular Panels (CRPs) is investigated. To numerically evaluate the performances of SST when generating wall-pressure plane waves (WPPWs) on CRPs, analytical developments are proposed to estimate the transfer functions between the monopole source and the CRPs. Two- and three-dimensional cases are considered and validated using the boundary element method. Then, parametric studies are carried out to determine the optimal parameters for implementing the SST process in two- and three-dimensional cases considering a conformal geometry, i.e., the array of monopoles has the same geometry as the structure of interest. The numerical results obtained are then supported by experimental investigations

*Corresponding author.
Email addresses: augustin.pouye@insa-lyon.fr (Augustin Pouye), cedric.maury@centrale-marseille.fr (Cédric Maury), laurent.maxit@insa-lyon.fr (Laurent Maxit)

using a robotized system to move the monopole source. The transfer functions obtained using the proposed analytical models are compared to the measured ones, yielding relatively good agreement between the results.

Keywords: Source Scanning Technique – Curved Rectangular Panels – Vibroacoustics – Wall-Pressure Synthesis – Diffuse Acoustic Field – Turbulent Boundary Layer – Wall-Pressure Plane Waves

1. Introduction

The experimental characterization of structures under random excitations such as the diffuse acoustic field (DAF) and the turbulent boundary layer (TBL) is of great interest in the building sector and the transportation industry [1, 2]. However, the test facilities generally used (i.e., reverberant chamber for the DAF and wind tunnel or *in situ* tests for the TBL) can be hard to control and costly. Moreover, the results obtained for a given structure can be very different from one facility to another, even though the same setup is implemented. The experimental synthesis of the vibroacoustic response of structures under stochastic excitations using an array of acoustic sources was theoretically demonstrated some decades ago by Fahy [3]. However, the technical limitations of this period did not allow the experimental validation of these techniques. Since 2000, several researchers have addressed this problem using various approaches. For instance; Maury *et al.* [4], Elliott *et al.* [5], Bravo and Maury [6] and Maury and Bravo [7] extensively discussed the real-time reproduction of random excitations using an array of loudspeakers. The experimental results obtained in the laboratory on different test cases clearly showed the ability of loudspeaker arrays to reproduce various partially correlated pressure fields, in particular for acoustic diffuse fields. Some years ago, the concept was even extended to an industrial application at the ZAL Center of Applied Aeronautical Research in Hamburg. The Acoustic Flight-Lab consists of a large semi-anechoic chamber including a 8.5-metre-long fuselage demonstrator excited with an array of 444 loudspeakers [8]. The setup is designed to replicate engine noise from propulsion concepts.

It is used to validate numerical models of cabin noise and to examine new noise reduction measures in the cabin [8, 9]. At present, approaches using an array of loudspeakers (which are controlled in real time) suffer from a significant drawback when the scale of the variations of the pressure field to be reproduced is small. This situation is encountered when considering a DAF excitation at relatively high frequencies (i.e. several kHz) or when considering a TBL excitation for which the convective contributions may be of small wavelengths. Instead, a criterion of at least 4 sources per minimum wavelength characterizing the targeted pressure field is commonly required to get an accurate synthesis [4, 5, 7]. When the frequency increases, the number of sources required may become very large. Moreover, the minimum distance between the sources is limited by the physical sizes of the loudspeakers considered. It is possible that the distance between the sources to respect the criterion can be smaller than the minimum distance permitted by the design of the array.

To circumvent this issue, Maury and Bravo [10] proposed a focused synthesis of TBL excitation over a sub-domain of the simulation surface. While this method allows reaching higher frequencies and ensures the correct reproduction of TBL excitation, it also limits the observation area to a fraction of the actual panel. To circumvent this issue, Marchetto et al. [11, 12] developed an alternative approach based on reciprocity principles. The first step consists in separating the contributions of the wall-pressure excitation from the vibroacoustic behavior of the panel through a mathematical formulation in the wavenumber domain. The excitation is then characterized by its cross-spectral density function whereas the vibroacoustic behavior of the panel is characterized by its sensitivity functions. These latter are measured experimentally, indirectly, using reciprocity principles. They are determined by exciting the structure at the point of interest and measuring the vibratory field with a laser vibrometer which is converted in the wavenumber space [11, 12]. The comparison of the results obtained with this approach versus the equivalent results from standard test facilities showed good agreement between both kinds of results as well as for DAF and TBL excitations. However, this approach can be experimentally time consuming for

estimating the transmission loss of a panel as it requires measuring the vibratory field of the panel for many source positions on a surface surrounding the panel. Aucejo et al. [13] took a different approach from the previous ones based either on the real-time control of a loudspeaker array [4–7] or on a reciprocity principle [11, 12]. Instead of using a compact source array with a predefined number of sources as in [4–7], only one monopole source was used along with the synthetic array principle [14]. The issue related to the size of the source was then overcome as in the indirect approach [11, 12]. However, contrary to the latter, the method used was "direct", which permits estimating the radiated pressure from the panel relatively easily.

The process proposed in [13] requires two identification steps and a post-processing step to simulate TBL-induced vibrations from a set of transfer functions and the synthetic array principle. The first identification step consists in characterizing the pressure field induced by the monopole source on the surface of the test structure. This operation should be repeated for each position of the source in the virtual array. This step may be time consuming but it should be carried out only once to characterize the source and its acoustical environment. The second identification step which should be repeated for each tested panel consists in measuring the transfer functions between the monopole source at the different positions on the virtual array and the receiving points of interest (on the panel or in the acoustic domain). The responses of the panel to unit wall-pressure plane waves (WPPWs), generally called the panel sensitivity functions [11, 12, 15], can be estimated during the post-processing step from the measured transfer functions using the monopole source. The last step consists in deducing the vibroacoustic response of the tested panel from the measured sensitivity functions and the cross-spectrum density function of the wall-pressure field characterizing the excitation.

This technique [13] was named the Source Scanning Technique (SST) and was applied to reproduce the vibration response of a steel panel to WPPWs or a TBL up to 300 Hz. A qualitative comparison of the response at a given point on the panel subject to a TBL excitation with measurements taken from the

literature was carried out. Globally, the results were encouraging. Recently, an extensive study of the SST process [16] was performed to definitively validate this experimental approach. To automate the process, a 3D Cartesian robot was used to move the acoustic source whereas a 2D Cartesian robot was used to move a linear array of microphones to measure the radiated pressure from the panel. The SST process was validated up to 2000 Hz for a simply supported aluminum panel by comparison with measurements in a reverberant room for the DAF and in an anechoic wind tunnel for the TBL excitation. Comparisons with an analytical model also showed that the technique is able to accurately estimate the sensitivity functions of the panel. For more complex panels, they may be helpful to extract the physical phenomena contributing to the noise radiation of the panels.

It can be highlighted that the principle of synthetic array used in [13] was originally developed for the aperture RADAR and was extended to the active aperture SONAR a long time ago [17, 18]. Although the principle was not new at the time of the works performed by Aucejo *et al.* [13], they were pioneers in the use of this principle to characterize a given panel excited by DAF or TBL excitation. Since then, other methods using this principle have been proposed for the same application. On one hand, the Wave Field Synthesis (WFS) approach [19] was extended in [20] for the reconstruction of random sound pressure distributions on a planar reproduction surface using a planar array of reproduction monopoles parallel to the reproduction plane. On the other hand, the Planar Nearfield Acoustic Holography (P-NAH) based on the fundamentals of acoustic holography was proposed in [21]. Both approaches are open-loop processes using arrays of acoustic sources. Experimental validations of these techniques coupled to the synthetic array principle are proposed in [22]. It was observed that they provided very good estimations of the transmission loss of the panel tested for the DAF and incident acoustic plane waves but were not able to accurately synthesize the wall-pressure field induced by a TBL excitation outside the acoustic wavenumber domain. The P-NAH approach [23] was extended to estimate the absorption coefficient of a sound absorbing material under a syn-

thesized DAF excitation at the material surface by using a synthetic array of acoustic monopoles facing the material. The estimated absorption coefficients for a melamine foam were in satisfactory agreement with those obtained from a model above 400 Hz. The frequency limitation could be explained by the finite size of the sample and the non-optimization of the virtual source array. The results of the method were then compared to measurements on a set of six typical acoustic materials using the standard reverberant room method [24]. Although its limitation in the low-frequency range was observed as in [23], it was shown that the method did not exhibit size effects as is generally seen with the reverberant room. Recently, two sound field synthesis methods for characterizing acoustic materials under plane wave excitation at arbitrary incidence angle [25] were studied. The first method consists of a real-time control of a set of loudspeakers to generate the plane waves whereas the second one is based on the synthetic array principle. It was observed that the first one permitted fast measurement once calibration was performed and that the results were better at high frequencies than the second one. The second method, however, was much simpler to install and use. It was studied in-depth and improved in a consecutive paper [26]. Emphasis was placed on the diffuse field sound absorption coefficient of the material. Contrary to the original concept based a spherical wave formalism [23], it was presented in a plane wave formalism. Moreover, the discrete version of the Paris formula was used to estimate the sound absorption coefficient. The proposed improvements overcome some of the limitations observed for the original version concerning the maximum incidence angle limit and when the distance from the source array to the microphone array is small. Techniques based on the synthetic array concept, such as SST, WFS, P-NAH, and their developments, have proven effective and precise in assessing the vibroacoustic response of Flat Rectangular Panels (FRPs) subjected to DAF or TBL excitation. Yet, within an industrial framework, the structures under consideration often exhibit more intricate geometries. For example, an aircraft's fuselage presents curvature in the direction perpendicular to the airflow, prompting the need to evaluate the curvature's impact on the vibroacoustic response

of curved structures to TBL excitation. Consequently, it is necessary to adapt these methodologies to more complex, non-academic entities such as Curved Rectangular Panels (CRPs). This paper aims to fulfil two interlinked goals in addressing this need.

- The first goal involves devising an analytical model for predicting the pressure field generated by a monopole source on the surface of Curved Rigid Panels (CRPs). This model diverges from the existing literature that typically considers a monopole positioned either outside [27] or inside [28, 29] a cylindrical surface. Instead, our model focuses on a monopole situated within a semi-infinite acoustic domain, delimited by a finite curved surface that transitions into infinite rigid baffles, as illustrated in Fig. 1. The formulation of this model enables the numerical examination of the precision of the synthesis method in reconstructing pressure fields on CRPs.

- The second objective focuses on evaluating the SST method's efficacy in generating sound pressure fields, such as WPPWs, on CRPs. This involves a numerical investigation into how the design of the array—specifically, its geometry, the spacing between virtual sources, and their proximity to the test structure - affects the accuracy of the sound pressure synthesized on the curved surface.

This paper is organized as follows

- In Sec. 2, analytical developments are proposed to compute the transfer functions between a monopole source and observation points located on a curved rectangular rigid surface. The solutions obtained for the two- and three-dimensional cases are verified numerically by comparison with boundary element simulations. The latter are much more computer time consuming than the proposed analytical solutions which are well-adapted for parametric studies of SST performances.

- The performances of the SST process for synthesizing WPPWs on curved surfaces are studied numerically in Sec. 3 from simulations using the

analytical solutions previously developed. Rules to define the optimal parameters of the virtual array of monopoles are extracted from these investigations.

- Finally, the results are experimentally verified in a controlled laboratory environment. The experimental setup is then presented in Sec. 4.1 and the experimental results are thoroughly discussed in Sec. 4.2.

2. Closed-form transfer functions

2.1. Description of the problem

A thorough search of the relevant literature did not yield any closed-form transfer functions between a monopole source located at a given point $\mathbf{x}_0$ and an observation point $\mathbf{y}$ located on a rigid curved surface (σ) as depicted in Fig. 1. This is required to build a theoretical model for the transfer functions used in the synthesis process over curved surfaces. The semi-infinite acoustic domain is bounded by the rigid curved surface (σ) which is extended by an infinite rigid flat baffle (β) (expanding at infinity along the x and $-x$ directions) whereas the Sommerfeld conditions are considered at infinity for the unbounded directions (i.e., non-reflecting boundary conditions).

It is underlined that in the following, the notations $\mathbf{x}$ and $\mathbf{y}$ refer to vector **points** in the spatial domain, be it in Cartesian or polar/cylindrical coordinates. The notations $\mathbf{x}\left(r,\theta\right)$ and $\mathbf{x}\left(r,\theta,z\right)$ (2D and 3D cases, respectively) for instance, should be read "point $\mathbf{x}$ of coordinates (r,θ) or point $\mathbf{x}$ of coordinates (r,θ,z)", respectively.

The previously described problem can be written in the following mathematical form with a time-domain convention $\mathrm{e}^{-\mathrm{i}\omega t}$

$$\begin{cases} \Delta p\left(\mathbf{x}\right) + k^2 p\left(\mathbf{x}\right) = -\delta\left(\mathbf{x}-\mathbf{x}_0\right), \mathbf{x} \in \Omega \\ \partial_{\mathbf{n}(\mathbf{x})} p\left(\mathbf{x}\right) = 0, \mathbf{x} \in \sigma \\ \lim\limits_{r\to\infty} r\left(\dfrac{\partial p}{\partial r} - \mathrm{i}kp\right) = 0, \mathbf{x} \in \Sigma_\infty \end{cases}, \tag{1}$$

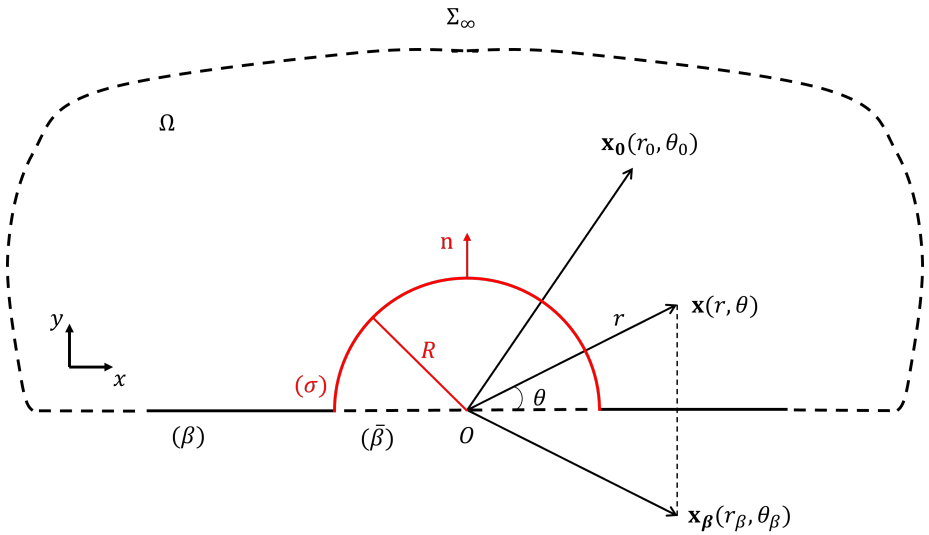

Figure 1: Problem geometry and parameters: (σ) represents the rigid curved surface, (β) the infinite rigid flat baffle, the monopole source is located at $\mathbf{x}_0$. For the three-dimensional case, refer to Fig. 2. Non-reflecting acoustic boundary conditions are specified on Σ_∞.

where $\partial_{\mathbf{n}(\mathbf{x})}\bullet$ designates the partial normal derivative at point $\mathbf{x}$ in the direction $\mathbf{n}$, and $\mathbf{n}$ corresponds to an exterior unit vector on the boundary constituted by $(\sigma \cup \beta)$. The domain of propagation Ω corresponds to the upper half-space delimited by the baffle (β) and the structure (σ) onto which wall sound pressures are reproduced.

In the following section, a function $p(\mathbf{x})$ is sought, which is the solution of the Neumann problem presented in Eq. (1). In the first step, the two-dimensional problem is solved and then follows the general three-dimensional case.

2.2. Two-dimensional case

In what follows, use will be made of the polar coordinates with the origin located at point O as shown in Fig. 1: the coordinates of any point $\mathbf{x}$ inside the propagation domain Ω are denoted by (r, θ); those of a monopole source at point $\mathbf{x}_0$ are denoted (r_0, θ_0) and those of a point $\mathbf{y}$ on $(\sigma \cup \beta)$ are denoted by $(r_\sigma, \theta_\sigma)$ in the polar coordinates. The subscript β in $\mathbf{x}_\beta$ and $\mathbf{x}_{0\beta}$ indicate the

image point with respect to the infinite rigid baffle plane (β).

Note that since $\mathbf{x}$ is closer to (σ) than $\mathbf{x}_0$ in our application, the result is $r < r_0$. From Eq. (3.51) in [30], Green's representation of the exterior sound pressure field $p(\mathbf{x})$ due to the source at point $\mathbf{x}_0$ and diffracted by the surface ($\sigma \cup \beta$) reads

$$p(\mathbf{x}) = p_0(\mathbf{x}) + \int_{\sigma\cup\beta} \mathrm{Tr}\left[\partial_{\mathbf{n}(\mathbf{y})} p(\mathbf{y})\right] G(\mathbf{x},\mathbf{y})\,\mathrm{d}S(\mathbf{y}) - \int_{\sigma\cup\beta} \mathrm{Tr}\left[p(\mathbf{y})\right] \partial_{\mathbf{n}(\mathbf{y})} G(\mathbf{x},\mathbf{y})\,\mathrm{d}S(\mathbf{y}), \quad (2)$$

where $\mathrm{Tr}[\bullet]$ represents the Cauchy trace operator and $\partial_{\mathbf{n}(\mathbf{y})}\bullet$ designates the partial normal derivative at point $\mathbf{y}$ in the direction $\mathbf{n}$.

In this application, the sound pressure should be predicted on or close to the curved surface. Therefore, only the case where $r < r_0$ (i.e., the receiving point is closer to the origin O than the monopole source) is considered.

Because the object is rigid, $\mathrm{Tr}\left[\partial_{\mathbf{n}(\mathbf{y})} p(\mathbf{y})\right] = 0$ on $\sigma \cup \beta$, and Eq. (2) reduces to

$$p(\mathbf{x}) = p_0(\mathbf{x}) - \int_{\sigma\cup\beta} \mathrm{Tr}\left[p(\mathbf{y})\right] \partial_{\mathbf{n}(\mathbf{y})} G(\mathbf{x},\mathbf{y})\,\mathrm{d}S(\mathbf{y}). \quad (3)$$

A priori, the Green's function G is chosen to be the following free-field Green's function

$$G(\mathbf{x},\mathbf{y}) = \frac{\mathrm{i}}{4} H_0^{(1)}\left[k_0 d(\mathbf{x},\mathbf{y})\right],\ \mathbf{x}\in\Omega \text{ and } \mathbf{y}\in\sigma\cup\beta,$$

where $H_0^{(1)}$ is the Hankel function of the first kind and order 0. In the following, the superscript "(1)" in the function considered will be omitted as only Hankel or Bessel functions of the first kind are used. $d(\mathbf{x},\mathbf{y})$ represents the distance (Euclidean norm) between point $\mathbf{x}$ and point $\mathbf{y}$.

It is important to note that $\partial_{\mathbf{n}(\mathbf{y})} G(\mathbf{x},\mathbf{y}) \neq 0$ on (β). Let us choose the half-space Green's function G_β whose normal derivative vanishes on the plane baffle ($\beta \cup \bar{\beta}$). It is given by

$$G_\beta(\mathbf{x},\mathbf{y}) = \frac{\mathrm{i}}{4} H_0^{(1)}\left[k_0 d(\mathbf{x},\mathbf{y})\right] + \frac{\mathrm{i}}{4} H_0^{(1)}\left[k_0 d\left(\mathbf{x},\mathbf{y}_\beta\right)\right], \quad (4)$$

where $\mathbf{x}_\beta$ is the mirror-image point of $\mathbf{x}$ with respect to the plane baffle. Thus, $\partial_{\mathbf{n}(\mathbf{y})} G_\beta(\mathbf{x},\mathbf{y}) = 0$ on $\beta\left(\cup\bar{\beta}\right)$. The integral representation in Eq. (3) reduces to

$$p(\mathbf{x}) = p_{0\beta}(\mathbf{x}) - \int_\sigma \mathrm{Tr}\left[p(\mathbf{y})\right] \partial_{\mathbf{n}(\mathbf{y})} G_\beta(\mathbf{x},\mathbf{y})\, \mathrm{d}S(\mathbf{y}), \tag{5}$$

where the integral term, which represents the sound field diffracted by $(\sigma \cup \beta)$ is now defined on a finite domain (σ) compared to Eq. (3) where the integration domain was composed of the structure (σ) and the infinite baffle (β). Note that the free-field source term $p_0(\mathbf{x})$ has been replaced by $p_{0\beta}(\mathbf{x}) = p_0(\mathbf{x},\mathbf{x}_0) + p_0(\mathbf{x},\mathbf{x}_{0\beta})$ such that $\partial_{\mathbf{n}(\mathbf{x})} p_{0\beta}(\mathbf{x}) = 0$ when $\mathbf{x} \in \beta \cup \bar{\beta}$.

The current problem conforms closely to cylindrical symmetry. Therefore, cylindrical harmonics expansion of the sound field are used for the sake of simplifying the search for a solution to the problem.

Let us proceed with a cylindrical harmonics expansion of $p_{0\beta}(\mathbf{x})$ and $\partial_{\mathbf{n}(\mathbf{y})} G_\beta(\mathbf{x},\mathbf{y})$.

- **Source term** $p_{0\beta}(\mathbf{x})$

  For $r < r_0$, it becomes (see Appendix D of Ref. [31])

  $$\frac{\mathrm{i}}{4} H_0^{(1)}\left[k_0 d(\mathbf{x},\mathbf{x}_0)\right] = \frac{\mathrm{i}}{4} \sum_{n=-\infty}^{+\infty} H_n(k_0 r_0)\, J_n(k_0 r)\, \mathrm{e}^{\,\mathrm{i}n(\theta-\theta_0)},$$

  where H_n and J_n are the Hankel function of the first kind and order n and the Bessel function of the first kind and order n, respectively. Note that $H_n J_n = H_{-n} J_{-n}$.

  The following equation is obtained using a similar expansion to the previous one

  $$\frac{\mathrm{i}}{4} H_0^{(1)}\left[k_0 d(\mathbf{x},\mathbf{x}_{0\beta})\right] = \frac{\mathrm{i}}{4} \sum_{n=-\infty}^{+\infty} H_n(k_0 r_{0\beta})\, J_n(k_0 r)\, \mathrm{e}^{\,\mathrm{i}n(\theta-\theta_{0\beta})} \text{ for } r < r_{0\beta}.$$

  Note that $r_{0\beta} = r_0$ and $\theta_{0\beta} = -\theta_0$. It follows that

  $$p_{0\beta}(\mathbf{x}) = \frac{\mathrm{i}}{4} \sum_{n=-\infty}^{+\infty} H_n(k_0 r_0)\, \mathrm{e}^{\,\mathrm{i}n\theta} \left[J_n(k_0 r)\, \mathrm{e}^{\,-\mathrm{i}n\theta_0} + J_n(k_0 r)\, \mathrm{e}^{\,\mathrm{i}n\theta_0}\right]. \tag{6}$$

  Using Euler's trigonometric formula yields

  $$p_{0\beta}(\mathbf{x}) = \frac{\mathrm{i}}{2} \sum_{n=-\infty}^{+\infty} H_n(k_0 r_0)\, J_n(k_0 r)\, \mathrm{e}^{\,\mathrm{i}n\theta} \cos(n\theta_0). \tag{7}$$

- **Derivative of the half-space Green's function $\partial_{\mathbf{n}(\mathbf{y})} G_\beta(\mathbf{x},\mathbf{y})$**

  G_β reads

$$G_\beta(\mathbf{x},\mathbf{y}) = \frac{\mathrm{i}}{4} H_0^{(1)}\left[k_0 d(\mathbf{x},\mathbf{y})\right] + \frac{\mathrm{i}}{4} H_0^{(1)}\left[k_0 d\left(\mathbf{x},\mathbf{y}_\beta\right)\right],$$

  where $\mathbf{y}(r_\sigma,\theta_\sigma)$ is now on (σ) exclusively. Note that $r > r_{\sigma\beta} = r_\sigma$. G_β can thus be written as

$$G_\beta(\mathbf{x},\mathbf{y}) = \frac{\mathrm{i}}{4}\sum_{n=-\infty}^{+\infty} H_n(k_0 r) J_n(k_0 r_\sigma)\,\mathrm{e}^{\,\mathrm{i}n(\theta-\theta_\sigma)} + \frac{\mathrm{i}}{4}\sum_{n=-\infty}^{+\infty} H_n(k_0 r) J_n(k_0 r_{\sigma\beta})\,\mathrm{e}^{\,\mathrm{i}n(\theta_{\sigma\beta}-\theta)}, \quad (8)$$

  and becomes

$$G_\beta(\mathbf{x},\mathbf{y}) = \frac{\mathrm{i}}{2}\sum_{n=-\infty}^{+\infty} H_n(k_0 r) J_n(k_0 r_\sigma)\,\mathrm{e}^{\,-\mathrm{i}n\theta}\cos(n\theta_\sigma). \quad (9)$$

  The partial normal derivative $\partial_{\mathbf{n}(\mathbf{y})}\bullet$ corresponds to the radial derivative in the polar coordinates $\partial_{r_\sigma}\bullet$, that is

$$\partial_{\mathbf{n}(\mathbf{y})} G_\beta(\mathbf{x},\mathbf{y}) = \partial_{r_\sigma} G_\beta(\mathbf{x},\mathbf{y}), \quad (10)$$

  and ultimately

$$\partial_{\mathbf{n}(\mathbf{y})} G_\beta(\mathbf{x},\mathbf{y}) = \frac{\mathrm{i}k_0}{2}\sum_{n=-\infty}^{+\infty} H_n(k_0 r) J_n'(k_0 r_\sigma)\,\mathrm{e}^{\,-\mathrm{i}n\theta}\cos(n\theta_\sigma), \quad (11)$$

  where the prime denotes the derivative with respect to the argument of the involved function.

Inserting Eqs. (7) and (11) into Eq. (5) yields

$$p(\mathbf{x}) = \frac{\mathrm{i}}{2}\sum_{n=-\infty}^{+\infty} H_n(k_0 r_0) J_n(k_0 r)\,\mathrm{e}^{\,\mathrm{i}n\theta}\cos(n\theta_0) - \frac{\mathrm{i}k_0}{2}\sum_{n=-\infty}^{+\infty} H_n(k_0 r)\,\mathrm{e}^{\,\mathrm{i}n\theta}\int_\sigma \mathrm{Tr}\left[p(\mathbf{y})\right] J_n'(k_0 r_\sigma)\cos(n\theta_\sigma)\, r_\sigma \mathrm{d}\theta_\sigma.$$

Let $A_n = \int_\sigma \mathrm{Tr}\left[p(\mathbf{y})\right] J_n'(k_0 r_\sigma)\cos(n\theta_\sigma)\, r_\sigma \mathrm{d}\theta_\sigma$ be the unknown amplitudes. The previous equation can be rewritten as follows

$$p(\mathbf{x}) = \frac{\mathrm{i}}{2} \sum_{n=-\infty}^{+\infty} H_n(k_0 r_0) J_n(k_0 r) \mathrm{e}^{\mathrm{i}n\theta} \cos(n\theta_0) - \frac{\mathrm{i}k_0}{2} \sum_{n=-\infty}^{+\infty} H_n(k_0 r) \mathrm{e}^{\mathrm{i}n\theta} A_n. \quad (12)$$

Let us determine $\partial_{\mathbf{n}(\mathbf{x})} p(\mathbf{x}) = \partial_r p(\mathbf{x})$. It reads

$$\partial_r p(\mathbf{x}) = \frac{\mathrm{i}k_0}{2} \sum_{n=-\infty}^{+\infty} H_n(k_0 r_0) J_n'(k_0 r) \mathrm{e}^{\mathrm{i}n\theta} \cos(n\theta_0) - \frac{\mathrm{i}k_0^2}{2} \sum_{n=-\infty}^{+\infty} H_n'(k_0 r) \mathrm{e}^{\mathrm{i}n\theta} A_n.$$

The Neumann boundary condition $\partial_{\mathbf{n}(\mathbf{x})} p(\mathbf{x})\big|_{\mathbf{x}=\mathbf{y}} = 0$ provides

$$\frac{\mathrm{i}k_0}{2} \sum_{n=-\infty}^{+\infty} H_n(k_0 r_0) J_n'(k_0 r_\sigma) \mathrm{e}^{\mathrm{i}n\theta_\sigma} \cos(n\theta_0) - \frac{\mathrm{i}k_0^2}{2} \sum_{n=-\infty}^{+\infty} H_n'(k_0 r_\sigma) \mathrm{e}^{\mathrm{i}n\theta_\sigma} A_n = 0. \quad (13)$$

A necessary condition for Eq. (13) to be satisfied requires

$$A_n = \frac{J_n'(k_0 r_\sigma)}{k_0 H_n'(k_0 r_\sigma)} H_n(k_0 r_0) \cos(n\theta_0). \quad (14)$$

Substituting Eq. (14) into Eq. (12), the sound pressure at any point $\mathbf{x} \in \Omega$ such that $r < r_0$ reads

$$p(\mathbf{x}) = \frac{\mathrm{i}}{2} \sum_{n=-\infty}^{+\infty} H_n(k_0 r_0) J_n(k_0 r) \mathrm{e}^{\mathrm{i}n\theta} \cos(n\theta_0) - \frac{\mathrm{i}k_0}{2} \sum_{n=-\infty}^{+\infty} H_n(k_0 r) \mathrm{e}^{\mathrm{i}n\theta} \frac{J_n'(k_0 r_\sigma)}{k_0 H_n'(k_0 r_\sigma)} H_n(k_0 r_0) \cos(n\theta_0).$$

Hence, the following analytical result is derived

$$p(\mathbf{x}) = \frac{\mathrm{i}}{2} \sum_{n=-\infty}^{+\infty} \mathrm{e}^{\mathrm{i}n\theta} \cos(n\theta_0) H_n(k_0 r_0) \left[J_n(k_0 r) - \frac{J_n'(k_0 r_\sigma)}{H_n'(k_0 r_\sigma)} H_n(k_0 r) \right]. \quad (15)$$

Eq. (15) can be seen as the transfer function between a field point $\mathbf{x} \in \Omega$ and a unit point source located at $\mathbf{x}_0$. However, the parameter of interest is the sound pressure at the surface of the curved structure (σ).

Using one of the Wronskian relations $J_n(\xi) H_n'(\xi) - H_n(\xi) J_n'(\xi) = \frac{2\mathrm{i}}{\pi\xi}$ (cf. [27], p. 21), the sought result, which corresponds to the sound pressure induced by

a monopole source at point $\mathbf{x}_0\,(r_0,\theta_0)$ and on a point $\mathbf{x}_\sigma\,(r_\sigma,\theta_\sigma)$ located on the rigid curved surface, is derived as follows

$$p\,(\mathbf{x}_\sigma) = -\frac{1}{\pi}\sum_{n=-\infty}^{+\infty} \mathrm{e}^{\,in\theta_\sigma}\cos\left(n\theta_0\right)\frac{1}{k_0 r_\sigma}\frac{H_n\,(k_0 r_0)}{H_n'\,(k_0 r_\sigma)}. \tag{16}$$

2.3. Three-dimensional case

Now, let us consider the three-dimensional case. The same assumptions as the 2D case are used; the only difference is that, the rigid curved structure is extruded in the z-direction (i.e. normal to the plane (x,y)). The problem to be solved consists of an infinite rigid half cylinder placed on a rigid infinite baffle plane and insonified by a monopole source located at $\mathbf{x}_0$ of coordinates (r_0,θ_0,z_0) as shown in Fig. 2. Mathematically, the 3D Helmholtz problem corresponds to Eq. (1) where Ω is the 3D semi-infinite acoustic domain bounded by the rigid surfaces.

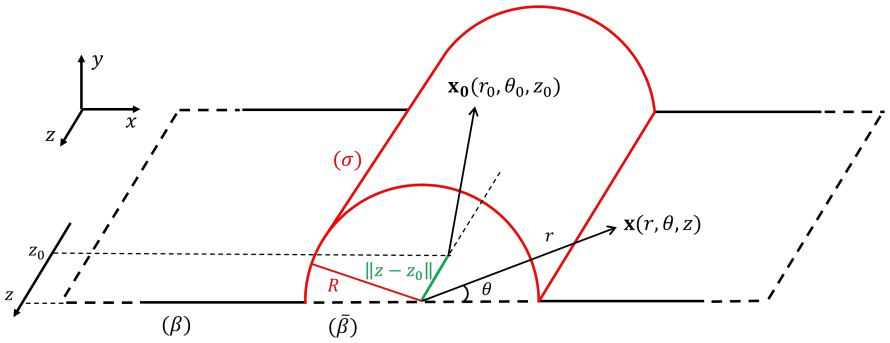

Figure 2: Problem geometry for the 3D case.

The total sound pressure field of the acoustic excitation due to a point source on a long half cylinder above/on a hard ground can be expressed as [27, 32]

$$p\,(\mathbf{x}) = p_0\,(\mathbf{x}) + p_{0\beta}\,(\mathbf{x}) + p_\sigma\,(\mathbf{x}) + p_{\sigma\beta}\,(\mathbf{x})\,, \tag{17}$$

where $p_0\,(\mathbf{x})$ and $p_{0\beta}\,(\mathbf{x})$ represent, respectively, the sound pressure field due to the monopole source and its image with respect to the ground while $p_\sigma\,(\mathbf{x})$ and $p_{\sigma\beta}\,(\mathbf{x})$ correspond to the scattered sound pressure field by the infinite half cylinder and its image with respect to the ground, respectively.

Using the standard Fourier transform about the z variable, the free field sound pressure generated by the monopole source

$$p_0(\mathbf{x}) = \frac{\mathrm{e}^{\,\mathrm{i}k_0\|\mathbf{x}-\mathbf{x}_0\|}}{4\pi\|\mathbf{x}-\mathbf{x}_0\|}, \tag{18}$$

can be expanded in terms of its Fourier integral representation as follows

$$p_0(\mathbf{x}) = \frac{\mathrm{i}}{8\pi}\sum_{n=-\infty}^{+\infty}\mathrm{e}^{\,\mathrm{i}n(\theta-\theta_0)}\int_{-\infty}^{+\infty}J_n(k_r r)\,H_n(k_r r_0)\,\mathrm{e}^{\,\mathrm{i}k_z(z-z_0)}\mathrm{d}k_z, \tag{19}$$

where $k_r = \sqrt{k_0^2 - k_z^2}$ corresponds to the axial wavenumber.

The same is done for the image of the source with respect to the ground/baffle. Hence, the following expression

$$p_{0\beta}(\mathbf{x}) = \frac{\mathrm{e}^{\,\mathrm{i}k_0\|\mathbf{x}-\mathbf{x}_{0\beta}\|}}{4\pi\|\mathbf{x}-\mathbf{x}_{0\beta}\|}, \tag{20}$$

is expanded as

$$p_{0\beta}(\mathbf{x}) = \frac{\mathrm{i}}{8\pi}\sum_{n=-\infty}^{+\infty}\mathrm{e}^{\,\mathrm{i}n(\theta-\theta_{0\beta})}\int_{-\infty}^{+\infty}J_n(k_r r)\,H_n(k_r r_{0\beta})\,\mathrm{e}^{\,\mathrm{i}k_z(z-z_{0\beta})}\mathrm{d}k_z. \tag{21}$$

Note that $r_{0\beta} = r_0$, $\theta_{0\beta} = -\theta_0$ and $z_{0\beta} = z_0$. Hence, it comes

$$p_{0\beta}(\mathbf{x}) = \frac{i}{8\pi}\sum_{n=-\infty}^{+\infty}\mathrm{e}^{\,\mathrm{i}n(\theta+\theta_0)}\int_{-\infty}^{+\infty}J_n(k_r r)\,H_n(k_r r_0)\,\mathrm{e}^{\,\mathrm{i}k_z(z-z_0)}\mathrm{d}k_z. \tag{22}$$

The sound pressure field scattered by the structure (σ) and its image with respect to the ground are respectively given in convenient forms as [27]

$$p_\sigma(\mathbf{x}) = \sum_{n=-\infty}^{+\infty}\mathrm{e}^{\,\mathrm{i}n\theta}\int_{-\infty}^{+\infty}A_n H_n(k_r r)\,\mathrm{e}^{\,\mathrm{i}k_z z}\mathrm{d}k_z, \tag{23}$$

and

$$p_{\sigma\beta}(\mathbf{x}) = \sum_{n=-\infty}^{+\infty}\mathrm{e}^{\,\mathrm{i}n\bar{\theta}}\int_{-\infty}^{+\infty}B_n H_n(k_r \bar{r})\,\mathrm{e}^{\,\mathrm{i}k_z z}\mathrm{d}k_z, \tag{24}$$

where $\bar{r}$ and $\bar{\theta}$ represent the coordinates of the field point with respect to the centerline of the image structure (σ_β), which is the same as that of the structure (σ) itself.

As (σ) and (σ_β) have the same centerline, it comes $\bar{r} = r$ and $\bar{\theta} = \theta$. Hence the total sound pressure scattered by the structure $p_s(\mathbf{x}) = p_\sigma(\mathbf{x}) + p_{\sigma\beta}(\mathbf{x})$ is

$$p_s(\mathbf{x}) = \sum_{n=-\infty}^{+\infty} \mathrm{e}^{\,\mathrm{i}n\theta} \int_{-\infty}^{+\infty} (A_n + B_n) H_n(k_r r)\, \mathrm{e}^{\,\mathrm{i}k_z z} \mathrm{d}k_z, \tag{25}$$

which will be simply written as

$$p_s(\mathbf{x}) = \sum_{n=-\infty}^{+\infty} \mathrm{e}^{\,\mathrm{i}n\theta} \int_{-\infty}^{+\infty} C_n H_n(k_r r)\, \mathrm{e}^{\,\mathrm{i}k_z z} \mathrm{d}k_z, \tag{26}$$

where $C_n = A_n + B_n$.

The total sound pressure field in Eq. (17) can now be expressed as

$$p(\mathbf{x}) = \frac{\mathrm{i}}{4\pi} \sum_{n=-\infty}^{+\infty} \mathrm{e}^{\,\mathrm{i}n\theta} \int_{-\infty}^{+\infty} \mathrm{e}^{\,\mathrm{i}k_z z} \cos(n\theta_0) J_n(k_r r) H_n(k_r r_0)\, \mathrm{e}^{\,-\mathrm{i}k_z z_0} - 4\pi\mathrm{i} C_n H_n(k_r r)\, \mathrm{e}^{\,\mathrm{i}k_z z} \mathrm{d}k_z. \tag{27}$$

The Neumann boundary condition $\left.\dfrac{\partial p(\mathbf{x})}{\partial r}\right|_{r=r_\sigma} = 0$ gives

$$C_n = \frac{1}{4\pi\mathrm{i}} \frac{J_n'(k_r r_\sigma)}{H_n'(k_r r_\sigma)} H_n(k_r r_0)\, \mathrm{e}^{\,-\mathrm{i}k_z z_0} \cos(n\theta_0). \tag{28}$$

Hence the sound pressure field of the acoustic excitation due to a monopole source on a long cylinder sector placed on rigid baffle can be written as

$$p(\mathbf{x}) = \frac{\mathrm{i}}{4\pi} \sum_{n=-\infty}^{+\infty} \mathrm{e}^{\,\mathrm{i}n\theta} \cos(n\theta_0) \int_{-\infty}^{+\infty} H_n(k_r r_0) J_n(k_r r) - \frac{J_n'(k_r r_\sigma)}{H_n'(k_r r_\sigma)} H_n(k_r r)\, \mathrm{e}^{\,\mathrm{i}k_z (z - z_0)} \mathrm{d}k_z. \tag{29}$$

Using the same Wronskian relation as for the 2D case leads to the following equation for the sound pressure on the surface of the structure itself at $r = r_\sigma$

$$p(\mathbf{x}_\sigma) = -\frac{1}{2\pi^2} \sum_{n=-\infty}^{+\infty} \mathrm{e}^{\,\mathrm{i}n\theta_\sigma} \cos(n\theta_0) \int_{-\infty}^{+\infty} \frac{1}{k_r r_\sigma} \frac{H_n(k_r r_0)}{H_n'(k_r r_\sigma)} \mathrm{e}^{\,\mathrm{i}k_z (z_\sigma - z_0)} \mathrm{d}k_z. \tag{30}$$

Note that Eq. (16) and Eq. (30) correspond to the sound pressure at point $\mathbf{x}_\sigma$ when a monopole of unit amplitude is located at point $\mathbf{x}_0$. In Sec. 3, this quantity will be named the transfer function between the monopole position $\mathbf{x}_0$

and the receiving point $\mathbf{x}_\sigma$ and will be denoted T_{ps}. These solutions are verified using comparisons with BEM results as presented in the subsequent section.

2.4. Verification of the analytical solutions

Now that Eq. (1) has been solved, the solutions of the two- and three-dimensional cases must be verified. The verification of these solutions is done using the Boundary Element Method (BEM) with OpenBEM [33] which is an open access code implemented in MATLAB. OpenBEM consists of three independent formulations: axisymmetrical (AxiBEM), bi-dimensional (2DBEM), and three-dimensional (3DBEM). They share a common structure and many of the features, but differ in the definition of the geometry and its implementation. Fig. 3 shows the mesh generated with *Gmsh 2.2*[1]: the mesh contained 12096 triangular elements (at least 5 elements per minimum wavelength) and a reflecting plane is defined at $z = 0$ in order to take into account the rigid flat baffle.

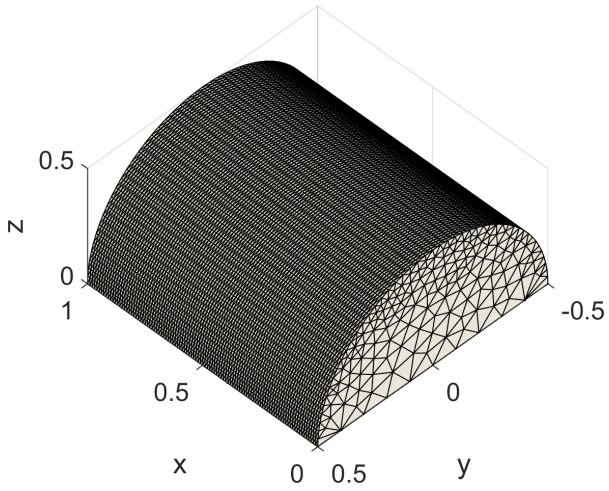

Figure 3: Generated mesh for OpenBEM numerical computations.

Naturally, 2DBEM is used for the verification of the two-dimensional trans-

[1] *Gmsh* is an open source 3D finite element mesh generator with a built-in CAD engine and post-processor [34].

fer functions and 3DBEM for that of the three-dimensional transfer functions. Comparing 2DBEM results to those provided by Eq. (16) shows a very good agreement between both methods, as shown in Fig. 4. In the case of the three-dimensional transfer functions, the results are also very accurate as is observed in Fig. 5. Although there are some minor discrepancies due to the limits of numerical methods (OpenBEM in this case), the solution established in Eq. (30) can be effectively validated.

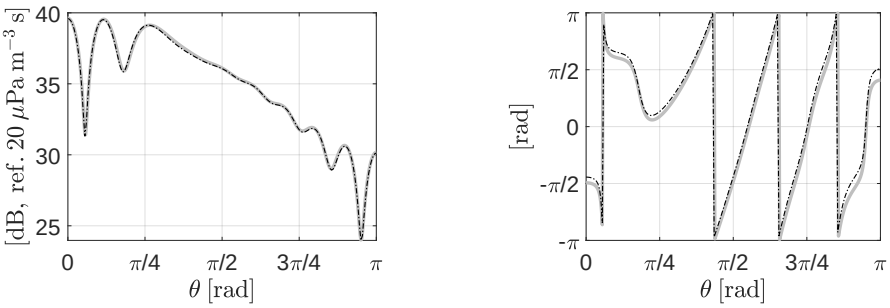

(a) (b)

Figure 4: Comparison between the amplitudes and phases of the wall sound pressure obtained with OpenBEM (gray continuous line) and those obtained using the analytical solution developed in Eq. (16) (dash-dotted black line) for one position of the monopole source $\left(r_0 = 1\,\mathrm{m}, \theta_0 = \frac{\pi}{4}\right)$ at a frequency $f = 1000\,\mathrm{Hz}$: two-dimensional case. (a) amplitudes (b) phases.

3. Parametric studies of the SST process performances

Prior to this study, the principle of SST process is recalled: starting from a set of monopole source positions around the structure of interest, a target sound pressure field will be generated on the surface of this structure (see Fig. 6). More precisely, the target sound pressure corresponds to a WPPW, expressed as $p(\mathbf{x}) = \mathrm{e}^{-\mathrm{i}\mathbf{k}\cdot\mathbf{x}}$. To achieve this, S different source positions are considered and the amplitudes of these sources will be determined so that the target sound pressure is reached at P observation points on the surface of interest. To assess

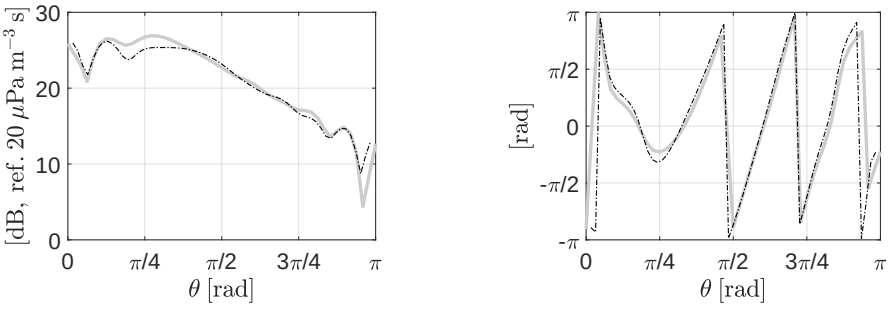

(a) (b)

Figure 5: Comparison between the magnitudes and phases of the wall sound pressure obtained with OpenBEM (gray continuous line) and those obtained using the analytical solution developed in Eq. (30) (dash-dotted black line) for one position of the monopole source $\left(r_0 = 0.6\,\mathrm{m}, \theta_0 = \frac{\pi}{4}, z_0 = 0.5\,\mathrm{m}\right)$ and at a frequency $f = 1000\,\mathrm{Hz}$: three-dimensional case. The distance along the z-axis between the plane of the monopole source and that of the observation points is $\|z - z_0\| = 0.3\,\mathrm{m}$.

the quality of the reproduction, Q reconstruction points are defined on the surface. To ensure the accuracy of the reproduction process, a check is performed to ensure that the Q reconstruction points are different from the P observation points by imposing $Q > P$, i.e., more reconstruction points than observation points. Additionally, the principle of the synthetic aperture is employed in order to use only a single monopole source. Instead of considering a set of S sources, a single source is moved to the S positions successively. Using the measured transfer functions for these S source positions and through post-processing, the behavior of the S source antenna is virtually recreated. The SST process can be summarized in three main steps [16]

- Characterization of the acoustic source: the transfer functions T_{ps} between the source positions s, and the observation points p on the curved surface are estimated (with the proposed analytical formulas in Sec. 2). $\mathbf{T}$ designates the transfer function matrix having the transfer functions T_{ps} as components.

- Computation of the source amplitudes: from the target sound pressure at the observation points which are stored in a sound pressure vector $\mathbf{p}$, the source amplitude vector $\mathbf{q}$ is obtained by inverting the following matrix equation

$$\mathbf{T}\mathbf{q} = \mathbf{p}. \tag{31}$$

When the number of observation points P is less than the number of source positions S, the system in Eq. (31) is under-determined and has an infinite number of solutions. However, when $P > S$, the system is over-determined and does not have a single exact solution. Nevertheless, a solution minimizing the reproduction error introduced in Eq. (36) can be established. The matrix $\mathbf{T}$ is thus rectangular, therefore Eq. (31) is solved in the least squares sense as

$$\mathbf{q} = \mathbf{T}^{\dagger}\mathbf{p}, \tag{32}$$

where the dagger symbol indicates the Moore-Penrose pseudo-inverse.

- Synthesis of the sound pressure field: the transfer functions T_{qs} between the source positions s, and the reconstruction points q on the curved surface are estimated and stored in the reconstruction transfer function matrix $\hat{\mathbf{T}}$. The synthesized sound pressure vector, $\hat{\mathbf{p}}$ containing the synthesized sound pressure at the reconstruction points is given by

$$\hat{\mathbf{p}} = \hat{\mathbf{T}}\mathbf{q}. \tag{33}$$

Here, the grids of observation points and reconstruction points are different, that is to say, $\hat{\mathbf{T}} \neq \mathbf{T}$ for testing the robustness of the reproduction process.

As mentioned above, in order to assess the quality and accuracy of the synthesis process, the sound pressure field is reconstructed using another grid of Q points. The transfer function matrices $\mathbf{T}$ and $\hat{\mathbf{T}}$ of respective size $P \times S$ and $Q \times S$ are determined through measurements or numerical simulations, with $Q > P$. The

vector of the reconstructed sound pressure $\hat{\mathbf{p}}$ is computed with the following expression: $\hat{\mathbf{p}} = \hat{\mathbf{T}}\mathbf{q}$.

3.1. Two-dimensional case

In this section, the goal is the reproduction of Wall-Pressure Plane Waves (WPPWs) of the form $p(\mathbf{x}) = \mathrm{e}^{-\mathrm{i}\mathbf{k}\cdot\mathbf{x}}$ where $\mathbf{k}$ is the wavevector characterizing the WPPW [35–37]. In the current geometry of the problem, illustrated in Fig. 6, the sound pressure induced by a WPPW at an observation point (on the structure) of angular coordinate θ takes the form

$$p(\mathbf{x}) = \mathrm{e}^{-\mathrm{i}k_\theta R\theta}, \tag{34}$$

where R is the radius of the structure and k_θ corresponds to the circumferential wavenumber characterizing the WPPW.

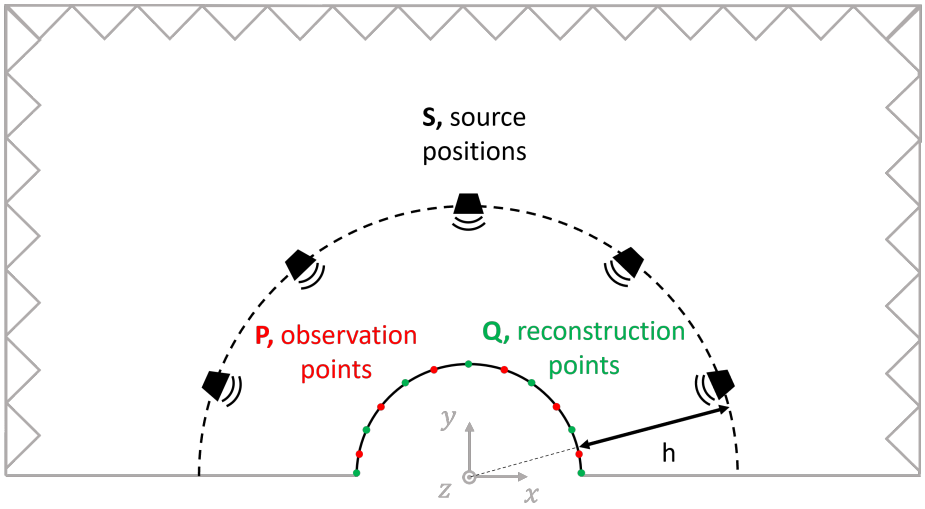

Figure 6: Section view of the SST setup for CRPs.

For the sake of simplicity, the structure of interest will be a half-circle with a radius $R = 0.5\,\mathrm{m}$. The observation points and the reconstruction points are uniformly distributed along the surface.

3.1.1. Studying the effect of the density of the array of monopoles

From the results obtained with planar structures [16], a good reproduction of the target sound pressure field was obtained when the criterion of 4 monopoles per minimum wavelength was fulfilled [7, 13]. However, in the current case, there is a curvature on the structure of interest, which means that this criterion has to be validated or changed for these structures. In this context, a study of the behavior of the SST process on these structures is proposed, successively fixing all other parameters but one: n_s, the number of required monopole sources per minimum wavelength. As stated earlier, the aim is the synthesis of WPPWs whose wavenumbers $k_\theta \in [-k_{\max}, k_{\max}]$ with $k_{\max}$ arbitrarily set at $50\,\mathrm{rad\,m^{-1}}$. It is important to note that uniform angular spacing between monopole positions is assumed. This spacing between two adjacent source positions is defined as a fraction of the lowest wavenumber to be synthesized at the highest frequency of interest

$$\delta_s = \frac{\lambda_{\min}}{n_s}, \tag{35}$$

where n_s is a positive integer representing the number of monopole positions per minimum wavelength.

In these studies, the geometry of the virtual array of monopoles is the same as the structure of interest as shown in Fig. 6 (i.e., the geometry is conformal to the structure, that is to say, circular). The radius of this arc of sources is always greater than the radius of the structure. In comparison to the *interplanar distance* [16] defined for rectangular structures, the *radial height* h is defined as the difference between the radius of the arc of monopoles and that of the structure. In the following, the radial height is $h = 5\,\mathrm{cm}$.

In order to assess the quality of the reproduction, an indicator, called the reproduction error, is defined as follows

$$e_p\left(k_\theta, \omega\right) = \frac{\mathrm{E}\left[\left\|\mathbf{p}\left(\mathbf{x}, k_\theta, \omega\right) - \hat{\mathbf{p}}\left(\mathbf{x}, k_\theta, \omega\right)\right\|^2\right]}{\left\|\mathbf{p}\left(\mathbf{x}, k_\theta, \omega\right)\right\|^2}. \tag{36}$$

In the previous equation, the dependence on k_θ and ω of the functions e_p, $\mathbf{p}$ and $\hat{\mathbf{p}}$ is explicitly indicated to provide a clear understanding of how the reproduction error is calculated.

Fig. 7 and Fig. 8 respectively show the reproduction error (see Eq. (36)) in the frequency-wavenumber domain and the real part of the target and synthesized sound pressure fields at the surface of the structure (θ designates the angular position of the considered point on the structure) for four different values of n_s.

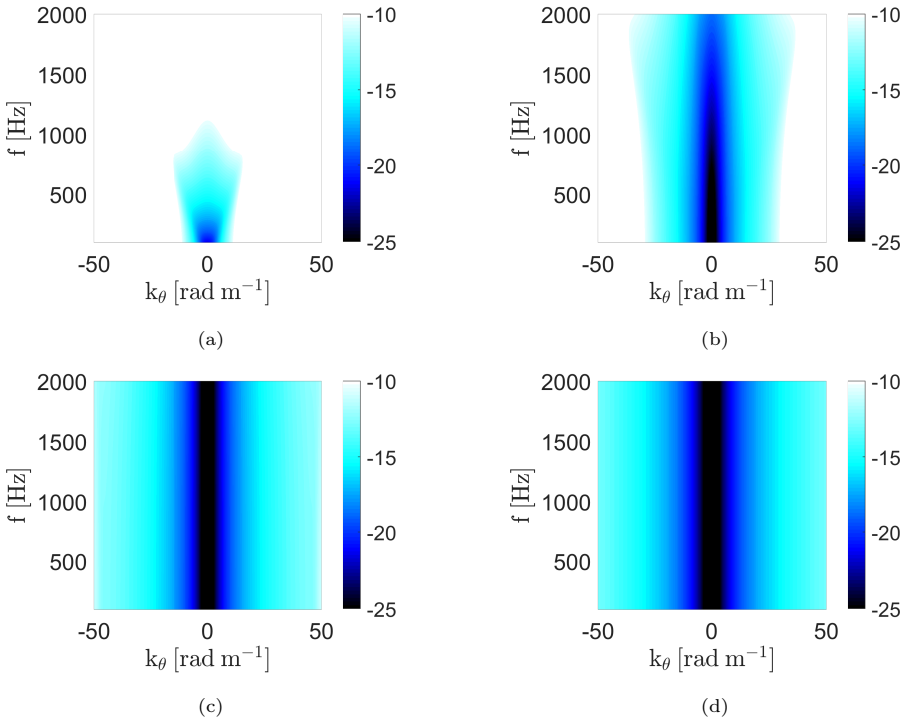

Figure 7: Reproduction error in the frequency-wavenumber domain: (a) $n_s = 1$, (b) $n_s = 2$, (c) $n_s = 3$ and (d) $n_s = 4$.

It is crucial to recall the reproduction error criteria for ensuring fidelity in the reproduction process, as outlined in Section 3.2.2 of [16]. The synthesis meets the accuracy standard if the reproduction error remains below -10 dB, meaning a relative Mean Square Error (MSE) of less than 10%.. Comparing Fig. 7a, Fig.

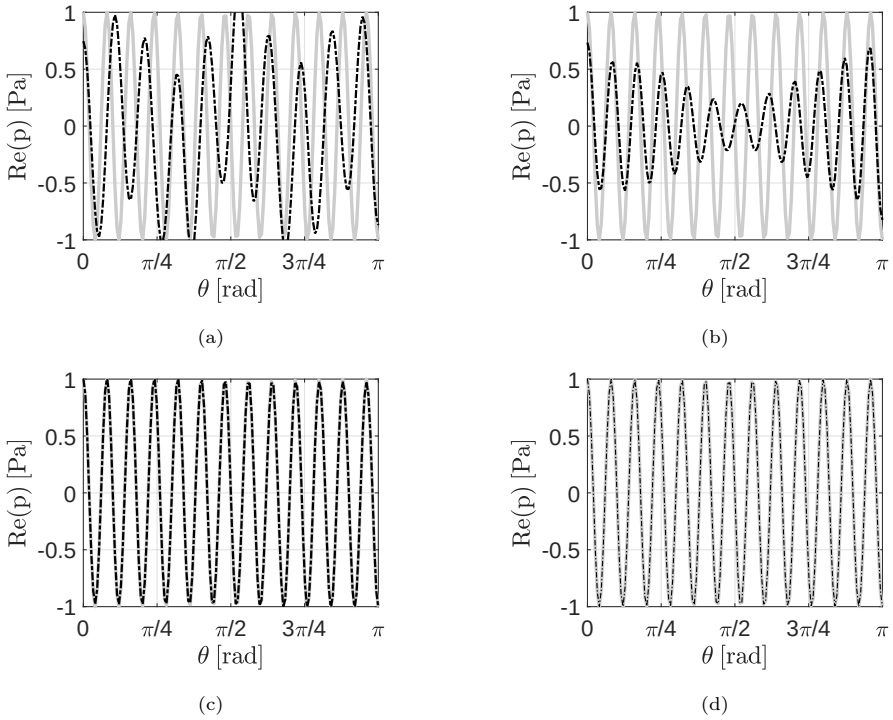

Figure 8: Real part of the target sound pressure field (continuous grey line) and the reconstructed sound pressure (dashed black line) of the WPPW defined by the wavenumber $k_\theta = 50\,\mathrm{rad\,m^{-1}}$ at a frequency $f = 2000\,\mathrm{Hz}$: (a) $n_s = 1$, (b) $n_s = 2$, (c) $n_s = 3$ and (d) $n_s = 4$.

7b, Fig. 7c and Fig. 7d, it can be noticed that the reproduction error covers an increasing area in the frequency-wavenumber domain when n_s varies from 1 to 4. This means that for an increasing number of monopoles per smallest wavelength, the reproduction process becomes more accurate. This observation is confirmed by comparing the target sound pressure fields and the synthesized ones. In Fig. 8a and Fig. 8b, the reproduced sound pressure fields do not match the target ones. However, in Fig. 8c and Fig. 8d, the reproduction process is very accurate and the synthesized sound pressure fields perfectly match the target ones. It is important to notice that only one example of WPPW is shown in these figures, the results for other WPPWs can be deduced by consulting the reproduction

error maps in Fig. 7 and choosing one frequency and one wavenumber.

In conclusion, the WPPWs are accurately synthesized when $n_s > 3$ which is consistent with the criteria that was defined for flat rectangular structures. Thus, the same criteria as in [16], that is $n_s = 4$, is defined for the remainder of this paper.

Let us now discuss the influence of the radial height on the conformal geometry setup of the SST process.

3.1.2. Influence of the radial height

Now that the criteria of four monopoles per smallest wavelength is verified, the influence of the radial height on the reproduction process can be studied by modifying its value and discussing the results in terms of two main indicators: the reproduction error and the condition number of the transfer function matrix $\mathbf{T}$ between each monopole position and the observation points on the structure. The condition number measures the sensitivity of the method with respect to perturbations in the input data and round-off error.

Three different values are considered for h: 5 cm, 10 cm, and 20 cm. For these three radial heights, the reproduction error in the frequency-wavenumber domain is very close to the one presented in Fig. 7d. At first sight, this suggests that the radial height has no influence on the quality of the synthesized sound pressure. However, it should be kept in mind that the transfer function matrix $\mathbf{T}$ between the monopole and the points on the curved surface are calculated numerically with the analytical formula in Eq. (16). They are then only perturbed by numerical errors induced by computing precision. In the SST process, the monopole amplitudes are obtained by inverting the transfer matrix $\mathbf{T}$ whose stability is assessed by the condition number.

Let us now take a look at the condition number of the transfer matrix $\mathbf{T}$ for each radial height in Fig. 9.

It can be noticed that the condition number does not vary that much as a function of the frequency. However, comparing the results for each of the radial heights, a rapidly increasing condition number is observed when the arc of

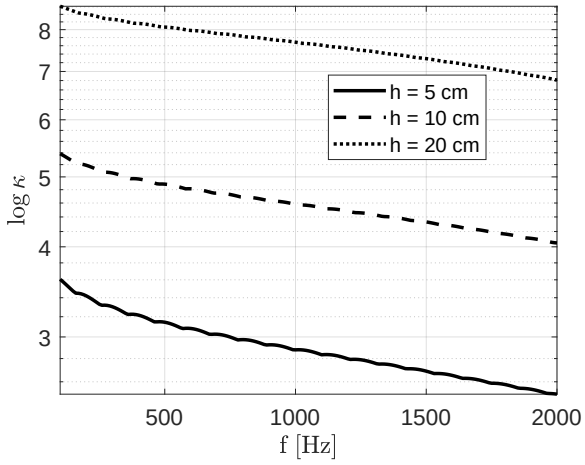

Figure 9: Condition number κ of the transfer matrix $\mathbf{T}$ for three different radial heights: $h = 5$ cm (continuous line), $h = 10$ cm (dashed line) and $h = 20$ cm (dotted line).

monopoles is displaced farther from the structure: from 10^3 for $h = 5$ cm to 10^9 for $h = 20$ cm. The condition number is a measure of the sensitivity of the sought parameters (i.e., the amplitudes of the monopole source at each position) with respect to perturbations in the input data and round-off errors made while solving Eq. (31) for $\mathbf{q}$. When the condition number is very large, the computed solution of the system may be in error. Values of the condition number near 1 indicate a well-conditioned matrix whereas large values indicate an ill-conditioned matrix. This means that the condition number of the transfer matrix must not be very high in practical applications. Otherwise, the errors induced by the hypothetical noise around the setup will be amplified due to the sensitivity of the system. The Tikhonov regularization method was used on the measured transfer matrices and the results showed an improvement of the condition number. However, the regularized transfer matrices did not yield a better reproduction error. As a result, the transfer matrices were directly used in the computation of the source amplitudes without any regularization.

In conclusion, the closer the arc of monopoles is to the structure (small values

of the radial height, $h = 5\,\text{cm}$ for instance), the lower the condition number of the transfer matrix, inducing a more accurate synthesis of the target sound pressure fields.

3.2. Three-dimensional case

Let us consider Fig. 6 with the z-axis as shown on the figure. In the three-dimensional case and considering the cylindrical coordinates, the target sound pressure at point $\mathbf{x}\,(R, \theta, z)$ corresponding to the WPPW of wavevector $\mathbf{k}\,(k_\theta, k_z)$ is of the form

$$p\,(\mathbf{x}) = \mathrm{e}^{\,-\mathrm{i}(k_\theta R\theta + k_z z)}, \tag{37}$$

where k_θ and k_z are the circumferential and the longitudinal wavenumbers, respectively.

The structure of interest is a rigid half-cylinder of 0.5 m radius and 1 m of length.

3.2.1. Influence of the density of the array of monopoles

Let us study the number of source positions n_s needed per minimum wavelength in order to achieve an accurate reproduction process.

Fig. 10 shows the reproduction error in the wavenumber domain for each value of n_s, for a frequency $f = 500\,\text{Hz}$. We recall that, for an accurate reproduction process, the reproduction error must be less than $-10\,\text{dB}$ which corresponds to an MSE of 10% between the target value and the reconstructed results.

When observing Fig. 10a, it can be noticed that the synthesis process is accurate when the wavevector of the WPPWs is in a circle of radius $12\,\text{rad}\,\text{m}^{-1}$. The quality of the reproduction exhibits the same trend in the longitudinal direction and in the circumferential one. For all other wavevectors and considering the set threshold of $-10\,\text{dB}$, the synthesis process is not accurate as the colorbar is set so that any reproduction error above $-10\,\text{dB}$ appears white in the wavenumber domain map.

Increasing the density of the monopole array from $n_s = 1$ to $n_s = 2$ (i.e., doubling the density) improves the process as the reproduction error decreases in the wavenumber domain map in Fig. 10b.

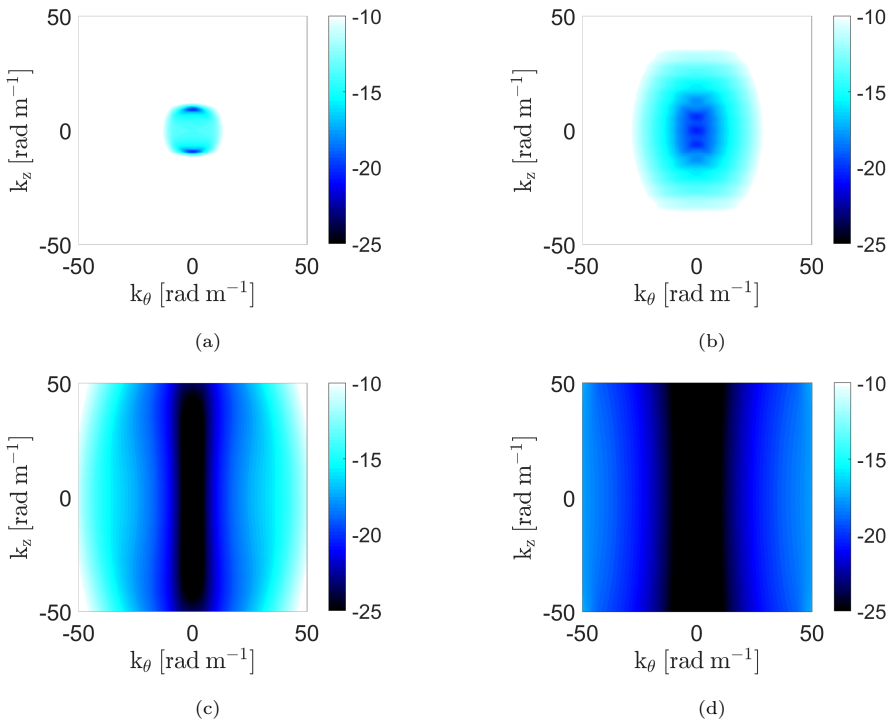

Figure 10: Parametric studies: influence of the density of the array of monopoles on the reproduction error e_p at a frequency $f = 500\,\mathrm{Hz}$. (a) $n_s = 1$, (b) $n_s = 2$, (c) $n_s = 3$ and (d) $n_s = 4$.

When looking at the wavenumber domain maps for $n_s = 3$ and $n_s = 4$ in Fig. 10c and Fig. 10d, respectively, a good reproduction process over almost all the wavevectors in the wavenumber domain of interest $[-50, 50] \times [-50, 50]$ rad^2 m^{-2}, is observed.

The parametric study was extended to additional frequencies, revealing trends similar to those observed in the two-dimensional case, although these results are not depicted here.

Fig. 11 illustrates the target WPPW intended for reconstruction through the SST process.

Now, let us take a look at the reconstructed sound pressure fields when n_s is consequently given values from the set $\{1, 2, 3, 4\}$.

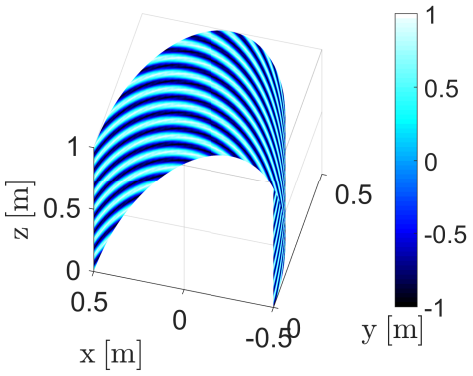

Figure 11: Target WPPW defined by the wavevector $(50, 50)$ rad m^{-1} and mapped on the surface of the half-cylindrical structure.

Fig. 12 represents plots on the surface of the half-cylinder of the reconstructed sound pressure field of the WPPW defined by the wavevector $(k_\theta, k_z) = (50, 50)$ rad m^{-1} and for a frequency $f = 500$ Hz.

As expected after the previous analysis of the reproduction errors for $n_s = 1$ and $n_s = 2$, the synthesized sound pressure fields do not match the target one as there are not enough monopole positions per minimum wavelength for an accurate SST process : this can be observed in Fig. 12a and Fig. 12b.

In Fig. 12c and Fig. 12d, the synthesized sound pressure fields match the target one for the frequencies of interest. There is no noticeable difference between the results obtained for $n_s = 3$ and those obtained for $n_s = 4$, which highlights that the reproduction error criterion of -10 dB is a severe one.

These comparisons allow us to state that at least 4 monopole positions per minimum wavelength are needed for an accurate reconstruction process.

Fig. 13 shows the reproduction error in the wavenumber domain for each value of n_s, for a frequency $f = 1000Hz$. The same conclusions as for Fig. 10 can be made, validating again the criteria on the number of monopoles per minimum wavelength.

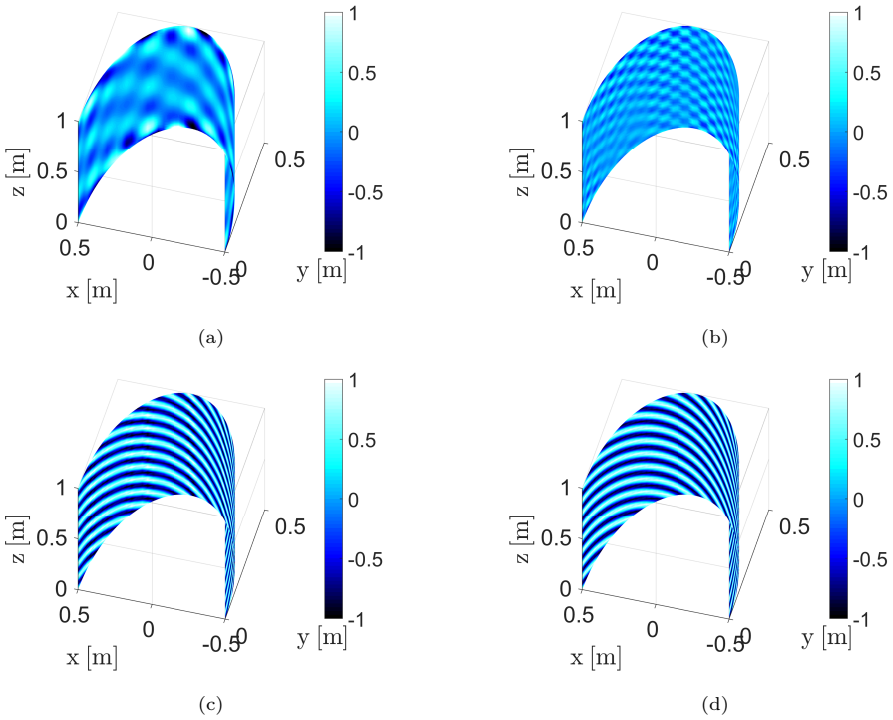

Figure 12: Parametric studies: influence of the density of the array of monopoles on the reconstructed sound pressure fields at a frequency $f = 500\,\text{Hz}$. (a) $n_s = 1$, (b) $n_s = 2$, (c) $n_s = 3$ and (d) $n_s = 4$.

3.2.2. Studying the effect of the radial height

Now, let's examine the impact of radial height h depicted in Fig. 6, considering the heights: $h = 5\,\text{cm}$ and $h = 10\,\text{cm}$. While the error maps for both heights at various frequencies are not displayed here, they closely resemble those seen in Fig. 13d. Notably, the reproduction error consistently remains below the $-10\,\text{dB}$ threshold, confirming the synthesis technique's accuracy for these radial heights.

Table 1 presents the condition numbers of the transfer matrix $\mathbf{T}$. The data illustrate that the condition number decreases as the frequency increases, consistent with observations in two-dimensional analyses. This reduction occurs at

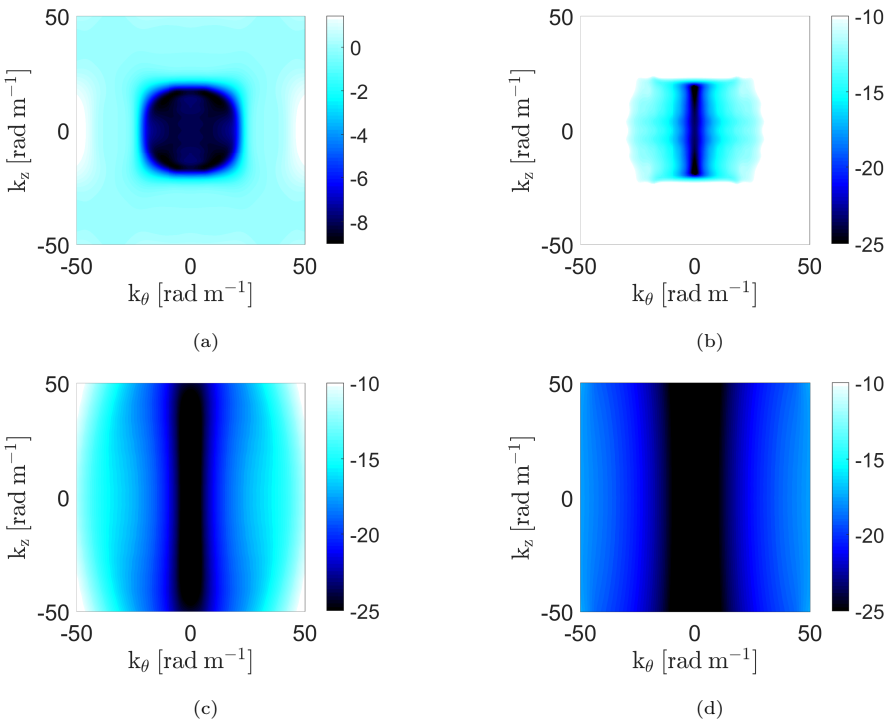

Figure 13: Parametric studies: influence of the density of the array of monopoles on the reproduction error e_p at a frequency $f = 1000$ Hz. (a) $n_s = 1$, (b) $n_s = 2$, (c) $n_s = 3$ and (d) $n_s = 4$.

a gradual rate with respect to frequency. Moreover, comparing radial heights of 5 cm and 10 cm shows minimal differences, suggesting that these dimensions negligibly influence the behavior of the condition number.

Table 1: Values of the condition number ($\log_{10}(\kappa)$) of the transfer matrix $\mathbf{T}$ for each frequency and radial height setup.

Frequency (Hz)	$h = 5$ cm	$h = 10$ cm
500	16.9	17
1500	16.6	16.7
2000	16.4	16.5

Although the condition number for a radial height of $h = 5\,\text{cm}$ slightly outperforms that of $h = 10\,\text{cm}$ across the three frequencies of interest, this observation aligns with previous results that indicated improvements when the distance between the monopole array and the structure is increased. It is important to note that the separation between the array and the structure should be at least equal to the spacing between two adjacent monopoles in the array. The results for $h = 20\,\text{cm}$ are not shown as they closely resemble those for $h = 5\,\text{cm}$ and $h = 10\,\text{cm}$, as depicted in Fig. 13d.

4. Experimental validation

In this section, the experimental transfer functions are compared to the analytical solutions (2D and 3D) of Sec. 2 for cross-validation.

4.1. Experimental setup

Let us consider Fig. 14 in which *chamber 1* designates the semi-anechoic room of the Laboratory of Mechanics and Acoustics (LMA) where the structure, the truss on which the monopole source is mounted, and the monopole source itself are present. The robot arm is mounted upside down on the truss structure for the needs of the experiment. This robot arm can slide along a motorized rail of length 2 m which is parallel to the z axis on Fig. 14.

The 2 m motorized rail is aligned with the centerline of the structure (half open cylinder) in order to have an accurate positioning of the robot arm with respect to the structure.

The monopole source is mounted on the robot using a 6 m flexible hose attached to a hollow aluminum tube attached to the free end of the robot arm, as shown in Fig. 15a.

The 63 microphones used during this experiment were flush-mounted on the rigid open half cylinder as shown in Fig. 15b. They were assembled per sets of 8 per external conditioner except one which had 7 microphones. Fig. 16 shows a picture of the type of microphone used and the conditioner they were connected to.

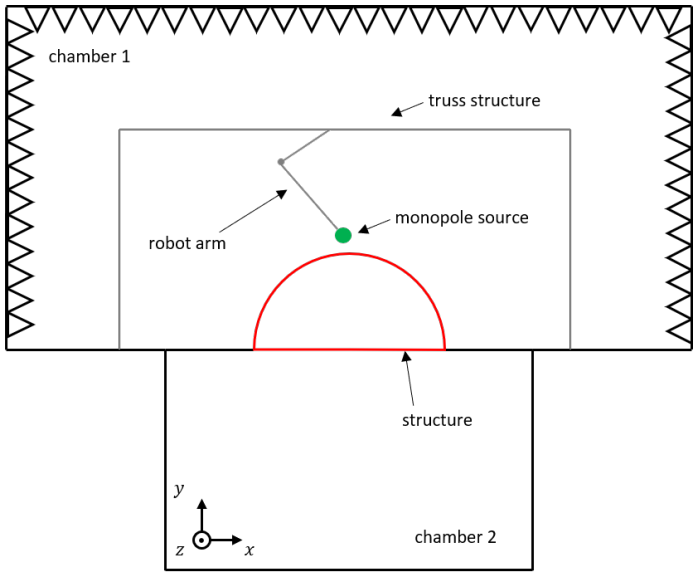

Figure 14: Sketch of the experimental setup for the SST process on CRPs.

All the cables installed in *chamber 1* and *chamber 2* were retrieved in a control room where they were plugged in an OROS acquisition system. *Chamber 1* corresponds to the semi-anechoic room and *chamber 2* is a reverberant room. The microphones were flush-mounted on a 5 cm thick plywood baffle, and we ensured acoustic isolation from *chamber 2* using a sealant around the microphone bodies. Consequently, any potential background noise from *chamber 2* has a negligible impact on the measurements. All the microphones were calibrated by taking into account the attenuation due to the length of the cables (estimated at 15 m) used to plug all the devices in the control room.

As the length of the cables were substantial, the first step corresponded to a quality control of the cables. A sinusoidal signal with a frequency of 200 Hz and an amplitude of 800 mV was sent. On the other side (control room), the same signal was received, but attenuated due to the resistivity of the cables, and this would have had an impact on the measurements if the microphones were not calibrated using the same experimental setup as for the measurement of the transfer functions.

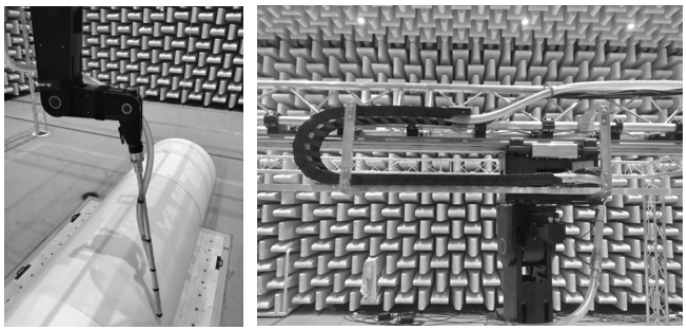

(a) Monopole source mounted on the robot arm.

(b) Flush-mounted microphones on the rigid open half cylinder.

Figure 15: Local views of the experimental setup.

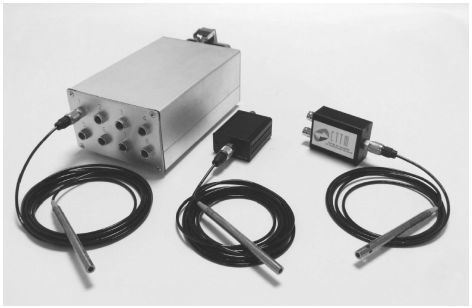

Figure 16: $1/4''$ microphones and 8 channel conditioner with a Harting connector output manufactured by the *Center for Transfer of Technologies of Le Mans* (CTTM).

Then each microphone was accurately calibrated using a piston-phone (GRAS, serial number: 23201, type 42AD) generating a signal of 113.99 dB at a frequency of 251.2 Hz. The microphones were successively placed inside the piston-phone using an adapter.

Fig. 17 shows the complete experimental setup used during the measurements.

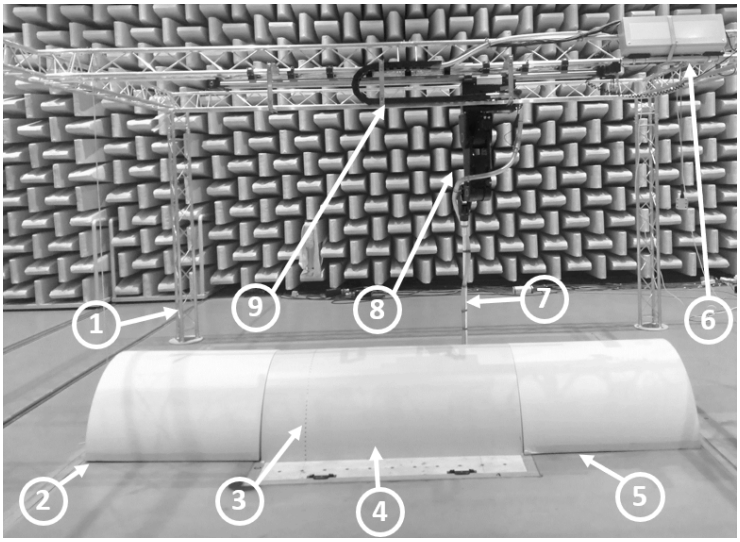

Figure 17: Experimental setup: simply supported rigid open half cylinder. The monopole source (7) is mounted on the robot arm (8) which can slide along the rail (9) and supported by the truss structure (1). The 63 microphones (3) are flush-mounted on the rigid open half cylinder (4) baffled by the half polystyrene cylinders (2) and (5). (6) corresponds to the robot arm control unit.

As shown in Fig. 15b, the microphone spacing is $\delta_p = 2\,\text{cm}$, ensuring a number of observation points P greater than the number of source positions S as $\delta_p > \delta_s \approx 3\,\text{cm}$. In order to avoid using a plethora of microphones for the measurement of the transfer functions, the idea is to apply the same "principle of invariance" as the one used for FRPs, see Appendix B of Ref. [16]. Certainly, the structure of interest is more complex than the flat panel but this invariance of the measurements should remain valid in this new case study in view of the symmetry of the system. This principle consists in using only one semi-circular microphone array to perform transfer function measurements over the entire surface of the half cylinder. Instead of having to move the microphone array (which is impossible in our configuration) or having a multitude of microphones to manage over the entire surface of the half cylinder, the monopole source is simply displaced to the position facing the location of the"virtual" array of

microphones where the transfer functions are to be measured.

Then, the transfer functions between each predefined source position and the flush-mounted microphones on the cylindrical structure are determined using a sweep signal from 1 to 2000 Hz with a linear sweep variation for a duration of 3 seconds and generated by the monopole source. These transfer functions will subsequently form the experimental transfer function matrix $\mathbf{T}_{\text{exp}}$ used later for sound pressure synthesis on the surface of the structure.

4.2. Validation of the transfer functions

This section is dedicated to the experimental validation of the two- and three-dimensional transfer functions previously established in Sec. 2.

4.2.1. Two-dimensional case

Fig. 18 presents a comparison between analytical and experimental transfer functions at two frequencies for a specified radial height and a monopole source position (r_0, θ_0). The comparison includes plots of the sound pressure along a semi-circular arc, which is experimentally represented by the arc of microphones labeled as (3) in Fig. 17 and visible in Fig. 15b.

Analysis of Fig. 18 reveals a strong correlation between the analytical results and the experimental measurements obtained using a 63-microphone array. These findings validate the two-dimensional theoretical transfer functions described in Eq. (16), which have also been compared with numerical results from OpenBEM.

4.2.2. Three-dimensional case

Similar to the two-dimensional case, the three-dimensional transfer functions outlined in Eq. (30) and the experimental setup described in Sec. 4.1 require validation through experiments. Fig. 19 illustrates comparisons between the theoretical transfer functions from Eq. (30) and actual measurements. These comparisons involve sound pressure plots on the structure's surface at various frequencies, a specific radial height, and two positions (r_0, θ_0, z_0) of the monopole

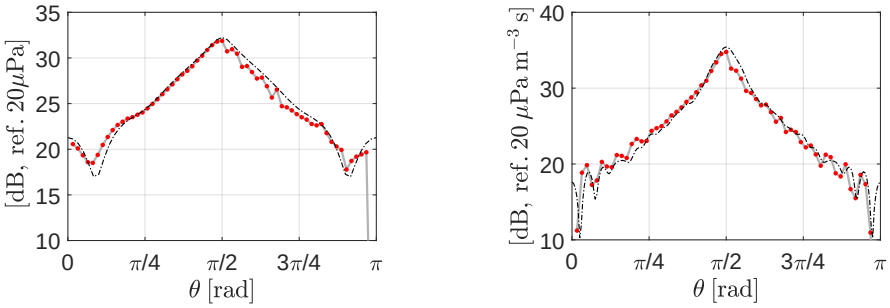

(a) $\theta_0 = \frac{\pi}{2}$ and $f = 500$ Hz

(b) $\theta_0 = \frac{\pi}{2}$ and $f = 2000$ Hz

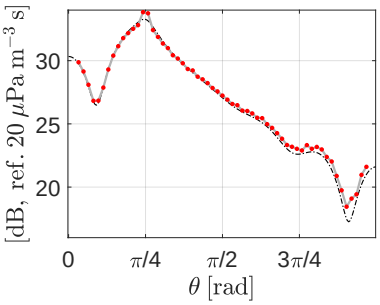

(c) $\theta_0 = \frac{\pi}{4}$ and $f = 500$ Hz

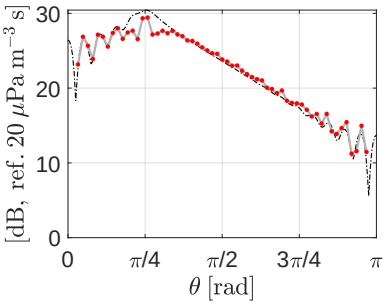

(d) $\theta_0 = \frac{\pi}{4}$ and $f = 2000$ Hz

Figure 18: 2D transfer functions for two angular positions θ_0 of the monopole source at two frequencies and a radial height $h = 5$ cm: comparison between the analytical results (dash-dotted black line) and the experimental measurements (continuous gray line, the red dots correspond to the position of the microphones) for the two-dimensional case.

source. Unlike the two-dimensional setup, the monopole source in the three-dimensional experiments is positioned on a different z-plane, not aligning with the microphone arc array's plane.

In Fig. 19a and Fig. 19b, the monopole source is located at

$$\left(r_0 = 55\text{ cm}, \theta_0 = \frac{\pi}{2}, z_0 = 50\text{ cm}\right),$$

and the microphone array is always at the same position. This figure shows that, despite some discrepancies, there is a good agreement between both types of results.

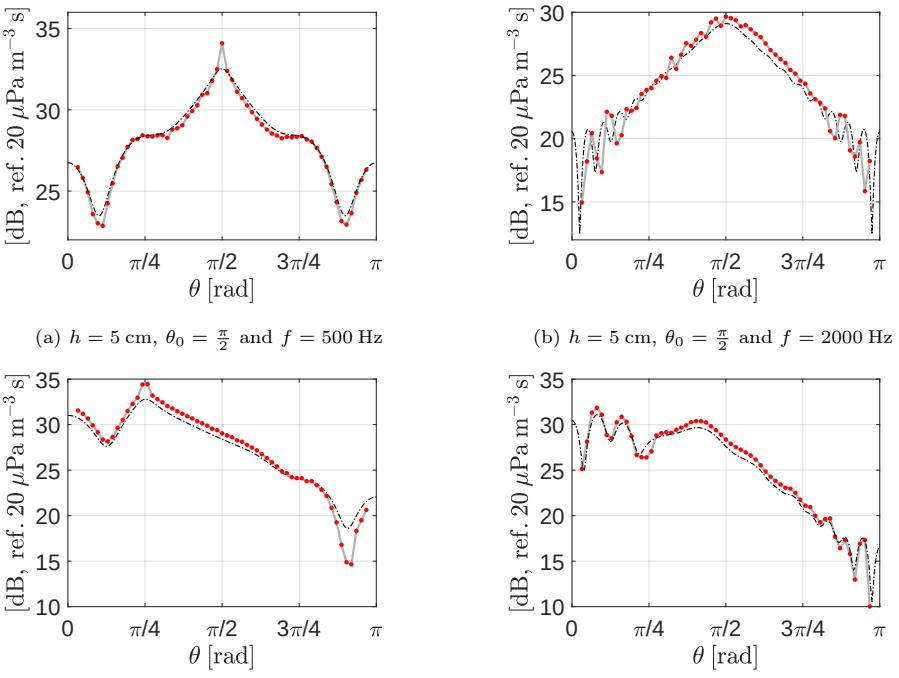

(a) $h = 5$ cm, $\theta_0 = \frac{\pi}{2}$ and $f = 500$ Hz

(b) $h = 5$ cm, $\theta_0 = \frac{\pi}{2}$ and $f = 2000$ Hz

(c) $h = 10$ cm, $\theta_0 = \frac{\pi}{4}$ and $f = 500$ Hz

(d) $h = 10$ cm, $\theta_0 = \frac{\pi}{4}$ and $f = 2000$ Hz

Figure 19: 3D transfer functions for two frequencies, two angular positions θ_0 of the monopole source and two radial heights. Comparison between the analytical results (dash-dotted black line) and the experimental measurements (continuous gray line, the red dots correspond to the position of the microphones) for the three-dimensional case. The observation points are on a different section from the plane/section of the source: $\|z - z_0\| = 50$ cm for the two top figures and $\|z - z_0\| = 25$ cm for the two bottom figures.

As for Fig. 19c and Fig. 19d, the monopole source is at position

$$\left(r_0 = 60\,\text{cm}, \theta_0 = \frac{\pi}{4}, z_0 = 25\,\text{cm}\right).$$

The data shows alignment with theoretical predictions, affirming the accuracy of the three-dimensional transfer functions. This comprehensive validation underscores the reliability of the theoretical framework.

5. Conclusions

This paper examines the adaptation of the Source Scanning Technique (SST) from Flat Rectangular Panels (FRPs) to Curved Rectangular Panels (CRPs). SST, an experimental method for characterizing structures under various excitations like the Diffuse Acoustic Field (DAF) and Turbulent Boundary Layer (TBL), utilizes a single moving acoustic source to simulate a full array and generate desired sound pressure fields. This technique offers a potential alternative or complement to traditional testing environments such as reverberant rooms or wind tunnels.

Despite an extensive review of the literature failing to produce any closed-form transfer functions for a curved rectangular panel with a monopole source above it, the initial approach was to solve the Helmholtz equation for this scenario. Transfer functions were developed for both two-dimensional and three-dimensional contexts. Verification was achieved through numerical simulations with OpenBEM, comparing the amplitudes and phases of surface sound pressures between analytical and numerical results, demonstrating strong concordance.

Following the numerical validation of the closed-form transfer functions, parametric studies were initiated to identify optimal design parameters for the virtual array of monopole sources to ensure precise reproduction. These studies, conducted for both two-dimensional and three-dimensional cases, utilized the reproduction error and the condition number of the transfer matrix as metrics to evaluate the synthesis process's quality and accuracy.

The study commenced by determining the minimum number of monopole positions needed in the array to accurately reproduce the target sound pressure field, identified as wall-pressure plane waves. It was found that at least four monopole positions per smallest wavelength are required for precise reproduction. Additionally, the relationship between the distance from the monopole array to the structure and the accuracy of reproduction was explored, revealing that a closer proximity enhances the reproduction quality, as long as it exceeds

the distance between adjacent monopoles.

After conducting initial studies to establish baseline parameters, the optimal settings for accurately reproducing the target sound pressure fields were determined. Subsequent steps involved the experimental validation of these transfer functions. The analytical and experimental transfer functions display strong agreement, confirming the validity of the closed-form transfer functions in both two-dimensional and three-dimensional contexts.

Further research should explore the practical implementation of the Source Scanning Technique (SST) and its application in the vibroacoustic characterization of curved elastic structures subjected to Diffuse Acoustic Field (DAF) or Turbulent Boundary Layer (TBL) excitations.

Acknowledgments

This work was funded by the French National Research Agency (VIRTECH project, ANR-17-CE10-0012) and performed in the framework of the LABEX CeLyA (ANR-10-LABX-0060) of Université de Lyon, France, as part of the program "Investissements d'Avenir" (ANR-16-IDEX-0005) supervised by the French National Research Agency (ANR).

References

[1] E. Ciappi, S. De Rosa, F. Franco, J.-L. Guyader, S. A. Hambric (Eds.), Flinovia - Flow Induced Noise and Vibration Issues and Aspects: A Focus on Measurement, Modeling, Simulation and Reproduction of the Flow Excitation and Flow Induced Response, Springer International Publishing, Cham, 2015.

[2] S. A. Hambric, A. D. Hanford, E. Ciappi, S. De Rosa, F. Franco, J. L. Guyader, R. C. K. Leung, Flinovia - Flow Induced Noise and Vibration Issues and Aspects-II: A focus on measurement, modeling, simulation and reproduction of the flow excitation and flow induced response, Springer International Publishing, 2018.

[3] F. J. Fahy, On simulating the transmission through structures of noise from turbulent boundary layer pressure fluctuations, Journal of Sound and Vibration 3 (1) (1966) 57–81.

[4] C. Maury, S. J. Elliott, P. Gardonio, Turbulent Boundary-Layer Simulation with an Array of Loudspeakers, AIAA Journal 42 (4) (2004) 706–713.

[5] S. J. Elliott, C. Maury, P. Gardonio, The synthesis of spatially correlated random pressure fields, The Journal of the Acoustical Society of America 117 (3) (2005) 1186–1201.

[6] T. Bravo, C. Maury, The experimental synthesis of random pressure fields: Methodology, The Journal of the Acoustical Society of America 120 (5) (2006) 2702–2711.

[7] C. Maury, T. Bravo, The experimental synthesis of random pressure fields: Practical feasibility, The Journal of the Acoustical Society of America 120 (2006) 2712–2723.

[8] P. Joshi, Y. Hoven, P. Cordes, Measurement and simulation combined high fidelity approach for studying aircraft cabin noise, in: Proceedings of DAGA, Hamburg, Germany, 2023.

[9] C. Hesse, P. Allebrodt, J.-N. Walther, Integration of multi-physics analysis into the cabin design process using virtual reality, in: AIAA AVIATION 2021 FORUM, 2021.

[10] C. Maury, T. Bravo, Focussed Synthesis of a Turbulent Boundary Layer Excitation, 22nd AIAA/CEAS Aeroacoustics Conference (May 2016).

[11] C. Marchetto, L. Maxit, O. Robin, A. Berry, Vibroacoustic response of panels under diffuse acoustic field excitation from sensitivity functions and reciprocity principles, The Journal of the Acoustical Society of America 141 (6) (2017) 4508–4521.

[12] C. Marchetto, L. Maxit, O. Robin, A. Berry, Experimental prediction of the vibration response of panels under a turbulent boundary layer excitation from sensitivity functions, The Journal of the Acoustical Society of America 143 (5) (2018) 2954–2964.

[13] M. Aucejo, L. Maxit, J. L. Guyader, Experimental simulation of turbulent boundary layer induced vibrations by using a synthetic array, Journal of Sound and Vibration 331 (16) (2012) 3824–3843.

[14] S. W. Autrey, Passive synthetic arrays, The Journal of the Acoustical Society of America 84 (2) (1988) 592–598.

[15] L. Maxit, M. Berton, D. Juvé, C. Audoly, Different vibro-acoustic models for predicting the flow-induced structural vibration and re-radiated noise, Springer International Publishing, 2013.

[16] A. Pouye, L. Maxit, C. Maury, M. Pachebat, Reproduction of the vibroacoustic response of panels under stochastic excitations using the source scanning technique, Journal of Sound and Vibration 510 (2021) 116307.

[17] L. J. Cutrona, Comparison of sonar system performance achievable using synthetic-aperture techniques with the performance achievable by more conventional means, The Journal of the Acoustical Society of America 58 (2) (1975) 336–348.

[18] L. J. Cutrona, Additional characteristics of synthetic-aperture sonar systems and a further comparison with nonsynthetic-aperture sonar systems, The Journal of the Acoustical Society of America 61 (5) (1977) 1213–1217.

[19] A. J. Berkhout, D. de Vries, P. Vogel, Acoustic control by wave field synthesis, The Journal of the Acoustical Society of America 93 (5) (1993) 2764–2778.

[20] A. Berry, R. Dia, O. Robin, A wave field synthesis approach to reproduction of spatially correlated sound fields, The Journal of the Acoustical Society of America 131 (2) (2012) 1226–1239.

[21] O. Robin, A. Berry, S. Moreau, Reproduction of random pressure fields based on planar nearfield acoustic holography, The Journal of the Acoustical Society of America 133 (6) (2013) 3885–3899.

[22] O. Robin, A. Berry, S. Moreau, Experimental vibroacoustic testing of plane panels using synthesized random pressure fields, The Journal of the Acoustical Society of America 135 (6) (2014) 3434–3445.

[23] O. Robin, A. Berry, O. Doutres, N. Atalla, Measurement of the absorption coefficient of sound absorbing materials under a synthesized diffuse acoustic field, The Journal of the Acoustical Society of America 136 (1) (2014) EL13–EL19.

[24] O. Robin, A. Berry, C. Kafui Amédin, N. Atalla, O. Doutres, F. Sgard, Laboratory and in situ sound absorption measurement under a synthetized diffuse acoustic field, Building Acoustics 26 (4) (2019) 223–242.

[25] S. Dupont, M. Sanalatii, M. Melon, O. Robin, A. Berry, J.-C. L. Roux, Characterization of acoustic materials at arbitrary incidence angle using sound field synthesis, Acta Acustica 6 (2022) 61.

[26] S. Dupont, M. Sanalatii, M. Melon, O. Robin, A. Berry, J.-C. L. Roux, Measurement of the diffuse field sound absorption using a sound field synthesis method, Acta Acustica 7 (2023) 26.

[27] E. A. Skelton, J. H. James, Theoretical Acoustics of Underwater Structures, Imperial College Press, 1997.

[28] C. R. Fuller, Monopole excitation of vibrations in an infinite cylindrical elastic shell filled with fluid, Journal of Sound and Vibration 96 (1) (1984) 101–110.

[29] J. James, Computation of Acoustic Power, Vibration Response and Acoustic Pressures of Fluid-Filled Pipes., Admiralty Marine Technology Establishment Teddington, 1982.

[30] P. Filippi, A. Bergassoli, D. Habault, J. P. Lefebvre, Acoustics: Basic Physics, Theory, and Methods, 1st Edition, Academic Press, San Diego, 1998.

[31] W. C. Chew, Waves and Fields in Inhomogeneous Media, IEEE Press, 1996.

[32] W. K. Lui, K. M. Li, The scattering of sound by a long cylinder above an impedance boundary, J. Acoust. Soc. Am. 127 (2) (2010) 12.

[33] V. C. Henríquez, P. M. Juhl, OpenBEM - An open source Boundary Element Method software in Acoustics, in: Proceedings of Internoise 2010, Lisbon, Portugal, 2010.

[34] C. Geuzaine, J.-F. Remacle, Gmsh: A 3-D finite element mesh generator with built-in pre- and post-processing facilities, International Journal for Numerical Methods in Engineering 79 (11) (2009) 1309–1331.

[35] L. Maxit, Simulation of the pressure field beneath a turbulent boundary layer using realizations of uncorrelated wall plane waves, The Journal of the Acoustical Society of America 140 (2) (2016) 1268–1285.

[36] M. Karimi, P. Croaker, L. Maxit, O. Robin, A. Skvortsov, S. Marburg, N. Kessissoglou, A hybrid numerical approach to predict the vibrational responses of panels excited by a turbulent boundary layer, Journal of Fluids and Structures 92 (2020) 102814.

[37] M. Karimi, L. Maxit, P. Croaker, O. Robin, A. Skvortsov, S. Marburg, N. Atalla, N. Kessissoglou, Analytical and numerical prediction of acoustic radiation from a panel under turbulent boundary layer excitation, Journal of Sound and Vibration 479 (2020) 115372.